J. Fluid Mech. (1999), *vol.* 387, *pp.* 177–204. Printed in the United Kingdom

© 1999 Cambridge University Press

Shear-flow instability in a rotating fluid

By J. A. VAN DE KONIJNENBERG, A. H. NIELSEN, J. JUUL RASMUSSEN AND B. STENUM

Risø National Laboratory, Optics and Fluid Dynamics Department, Building 128, P.O. Box 49, DK-4000 Roskilde, Denmark

(Received 13 November 1997 and in revised form 22 December 1998)

The instability of a forced, circular shear layer in a rotating fluid has been studied experimentally and numerically. The experiments were performed with a shallow layer of water in a parabolic tank, in which it is possible to apply radial pumping and to model a geophysical beta-effect. A shear layer was produced by a secondary rotation of the central part of the parabolic vessel. In most experiments, the shear layer takes on the appearance of a sequence of vortices, the number of which decreases with increasing strength of the shear. A beta-effect may prevent the formation of a steady vortex chain. Continuous pumping of fluid from the periphery to the centre or vice versa leads to an azimuthal velocity field corresponding to a point vortex. This azimuthal flow appears to stabilize the shear flow if it is opposite to the inner rotation, and to be destabilizing otherwise.

The numerical investigations consist of the solution of the quasi-geostrophic equation in a geometry similar to the experimental situation and with a term modelling the experimental forcing. Though the numerical computations are based on a two-dimensional model, they capture the essential features of the instability and the resulting vortex structures.

1. Introduction

The present paper concerns the nonlinear evolution of a circular shear layer in a rotating fluid. This subject is an extension of the symmetric split-disk problem analysed by Stewartson (1957) to a differential rotation that is still small compared with the rotation of the background, but large enough to make the shear layer unstable. Typically, an unstable shear layer is transformed into a number of columnar vortices which settle down to a stable symmetric configuration, but interesting variations such as subharmonic modulations and travelling disturbances can occur.

In 1967, Hide & Titman performed experiments with a rotating tank, equipped with a suspended differentially rotating disk. They reported instability above a well-defined threshold, leading to the final mode number decreasing with the amplitude of the differential rotation. Rabaud & Couder (1983) and later Chomaz *et al.* (1988) presented results obtained in a thin layer of air between two plates; the latter paper also includes numerical results. In their study the fluid layer is thinner than the Ekman layer thickness, so no Stewartson-type layers are involved. Nevertheless, bottom friction is represented by a similar to that term in the equation of motion in the case of Ekman damping, and the phenomena they observed are comparable to those of Hide & Titman. More results about the nonlinear shear layers were presented by Niino & Misawa (1984), in particular in relation to the initial instability. The set-up they used was similar to that of Hide & Titman in the sense that the fluid depth is

https://doi.org/10.1017/S0022112099004887 Published online by Cambridge University Press

much larger than the thickness of the Ekman layer. In their experiments the flow is driven by a very thin disk at the bottom of the tank, which offers the advantage of an almost uniform depth. Their paper also includes a discussion of additional references not mentioned here.

Nonlinear shear layers in a rotating fluid are only partially understood theoretically. Niino & Misawa (1984) applied linear stability analysis to the initially circular shear layer, including viscous diffusion and Ekman pumping. Their theoretical results predicted the critical Reynolds number and wavenumber, and were in good quantitative agreement with experimental observations. However, the initial instability does not always correspond to the final state. For instance, Niino & Misawa found that according to the concept of the fastest growing unstable mode, the wavenumber (and therefore the number of vortices) should increase with increasing Reynolds number. However, it is an established experimental result that the number of vortices in the final state decreases with the amplitude of the applied shear.

Progress has been made in the analysis of the shear layer with weakly nonlinear theory (see Churilov & Shukhman 1992; Bergeron *et al.* 1996; and the review paper by Dolzhanskiĭ, Krymov & Manin 1990). In this approach, the disturbance with respect to a circular flow is expanded in a small parameter corresponding to the nonlinearity of the system. This theory accounts for certain experimentally observed phenomena such as hysteresis and saturation of the amplitude of the unstable wave mode, but is limited to flows that are only slightly supercritical. If the supercriticality is not small, the initial shear layer is transformed into vortices that start to interact and merge, a process that leads to a final structure that is hardly related to the initial instability (see e.g. numerical simulations by Bergeron *et al.* 1996). In this respect, a scaling argument by Manin (1990) seems to provide a more adequate description. Manin estimated the length scale of the vortices based on a Kolmogorov wavenumber spectrum and the presence of 'external' friction (which may be dissipation by Ekman pumping or the friction experienced by a very thin layer between two plates). The scaling predicts a decrease of the number of vortices with the Reynolds number in a way that fits well with experimental data. However, much has still to be learned about the structure and properties of the final state, and the evolution from the initial instability to the final state.

The evolution of a shear layer between two rotating plates with a differentially rotating inner section is a prototype case for the behaviour of the boundary of a forced vortex. The examples that inspired our investigations are the atmospheric vortices present around the North and South Poles (see e.g. McIntyre 1989; Waugh *et al.* 1994). Although we do not aim at a direct comparison with the geophysical situation, we do include a latitude-dependence of the Coriolis parameter. Our goal has been to investigate experimentally and numerically the properties of a shear layer both with and without effects mimicking the gradient in the Coriolis parameter. The experiments were performed in a shallow layer of water in a rotating vessel with a parabolic shape and a differentially rotating central section. By rotating the vessel with the right angular velocity, a water layer with a uniform vertical thickness can be created. A slightly higher or lower angular velocity leads to a radial dependence of the depth, which leads to similar effects as the variation in the Coriolis parameter in the Earth's atmosphere. Moreover, we studied the influence of an additional vorticity-free shear flow, induced by continuous pumping of fluid from the periphery to the the centre of the differentially rotating disk. The numerical simulations consist of the solution of the two-dimensional vorticity equation, including a term representing Ekman pumping (thereby accounting for the forcing by the rotation of the central

https://doi.org/10.1017/S0022112099004887 Published online by Cambridge University Press

bottom part) and a term representing the gradient in the Coriolis parameter according to the β-plane approximation.

The further organization of this paper is as follows. In § 2, an overview of the theoretical background is given, and the most important quantities are defined. In §§ 3 and 4, the experiments are described and discussed. The numerical method and the results of the simulations are treated in §§ 5 and 6. A summary of the conclusions is given in § 7.

2. General theory and background

2.1. *Rotating flows*

Consider the three-dimensional Navier–Stokes equation for an incompressible barotropic flow in a system rotating around a vertical axis with angular velocity $\boldsymbol{\Omega}$:

$$\frac{\partial \boldsymbol{v}}{\partial t} + (\boldsymbol{v}\cdot\nabla)\boldsymbol{v} = -\frac{1}{\rho}\nabla p - 2\boldsymbol{\Omega}\times\boldsymbol{v} + \nu\nabla^2\boldsymbol{v} \tag{2.1}$$

where $\boldsymbol{v}$ is the fluid velocity, ν is the kinematic viscosity, and p is the pressure relative to the background pressure field $\frac{1}{2}\rho\Omega^2 r^2 - \rho g z$ due to the rotation and the gravitational acceleration. An important limiting case is the so-called geostrophic balance, described by an equilibrium between the pressure term $-(1/\rho)\nabla p$ and the Coriolis term $-2\boldsymbol{\Omega}\times\boldsymbol{v}$. It can be shown (see e.g. Greenspan 1968; Pedlosky 1987) that in geostrophic balance, the flow field does not vary along the rotation axis, a phenomenon known as the Taylor–Proudman theorem. First, consider a layer with a flat bottom and a free surface with negligible curvature; in that case the flow is strictly horizontal. By taking the vertical component of the curl of (2.1) we arrive at an equation for the scalar vorticity ω in a rotating system:

$$\frac{\partial \omega}{\partial t} + \boldsymbol{v}\cdot\nabla\omega = \nu\nabla^2\omega \tag{2.2}$$

where $\boldsymbol{v}$ and ∇ are now vectors in the horizontal plane. Although two-dimensionality breaks down as the ageostrophic terms in reality become too large, it has been shown by numerous experiments to be a fairly robust feature of rotating flows (see e.g. Hopfinger & van Heijst 1993).

One important parameter is the Rossby number Ro, representing in general the motion *in* the rotating system relative to the motion *of* the rotating system. In the present paper, we define the Rossby number as $\Delta\Omega/\Omega$, with Ω the rotation of the system in the absence of differential rotation, and $\Delta\Omega$ the angular velocity of the differential rotation. This inner rotation is called cyclonic if $Ro > 0$, and anticyclonic if $Ro < 0$. If the Rossby number is negligible, the advective term in (2.1) is small with respect to the pressure gradient and the Coriolis force.

2.2. *Ekman layers*

The presence of friction with the bottom gives rise to an Ekman boundary layer, in which the horizontal flow field is matched with the velocity of the bottom plate. The Ekman layer is a viscous boundary layer, in which the geostrophic balance no longer applies. Outside the Ekman layer, the flow is still approximately geostrophic; this region is called the interior. The Ekman layer influences the interior by imposing a weak vertical velocity component just outside the layer. It can be shown analytically (Greenspan 1968; Pedlosky 1987) that if the advective term is negligible, the upward Ekman pumping velocity is given by $\frac{1}{2}\delta(\omega - \omega^*)$ with $\delta = (\nu/\Omega)^{1/2}$ being the thickness

https://doi.org/10.1017/S0022112099004887 Published online by Cambridge University Press

of the Ekman layer, ω the vorticity of the fluid in the interior, and ω^* the vorticity of the bottom plate. The thickness δ is often written as $E^{1/2}H$, with H the depth of the fluid and $E = \nu/\Omega H^2$ the Ekman number. The weak vertical velocity component induced by the bottom friction leads to a stretching or squeezing of fluid columns above the Ekman layer, and therefore to a increase or decrease in interior vorticity. For fluid rotating with background rotation Ω, this increase is given by $\partial\omega/\partial t = 2\Omega\partial w/\partial z$, with w being the vertical component of the velocity. For a free-surface fluid layer with depth H, this results in an adaptation of the vorticity equation for the interior fluid according to

$$\frac{\partial\omega}{\partial t} + \boldsymbol{v}\cdot\nabla\omega = \lambda(\omega^* - \omega) + \nu\nabla^2\omega. \tag{2.3}$$

with $\lambda = (\nu\Omega)^{1/2}/H$. An important limiting case of the equation above is the decay of a vortex due to Ekman pumping if the advective term is negligible. In that case, Ekman pumping leads to exponential decay of the vorticity field on a time scale $\tau = 1/\lambda$. Depending on the sign of the relative vorticity, this decay is referred to as linear spin-up or spin-down.

2.3. *Stewartson layers*

In the case of a differentially rotating bottom, ω^* acts as a forcing term. A mathematically tractable example of a forced vortex is the equilibrium between the Ekman term and the viscous term if the bottom is in solid-body rotation with angular velocity Ω outside a given radius a, and in differential solid-body rotation with $\Omega + \Delta\Omega$ within $r = a$. The discontinuity in the velocity of the fluid is then smeared out over a layer with thickness $E^{1/4}H$, known as the Stewartson $E^{1/4}$-layer (Stewartson 1957; Greenspan 1968). This layer lifts the discontinuity in the azimuthal velocity, but still leaves a discontinuity in the radial component of the velocity. In reality, there appears to be an inner boundary layer with thickness of the order of $E^{1/3}H$ in which vertical transport takes place. This $E^{1/3}$-layer falls outside the scope of a two-dimensional modelling, and we will not consider it further.

According to the theory of Niino & Misawa (1984), the stability of the Stewartson layer is determined by the Reynolds number

$$Re = \frac{a\Delta\Omega d}{2\nu} \tag{2.4}$$

with d the thickness of the shear layer, given here by $E^{1/4}H$ (note that our expression for the shear width d is different from that of Niino & Misawa by a factor $\sqrt{2}$ because of the difference between a free surface and a rigid lid). The Reynolds number may be expressed in terms of Ro and E according to $Re = \frac{1}{2}RoE^{-3/4}aH^{-1}$.

2.4. *Analogy with flow between parallel plates*

Rabaud & Couder (1983) and Chomaz *et al.* (1988) performed experiments in a layer of air between horizontal plates separated by a small distance e, forced into a shear layer by a simultaneous differential rotation of both plates. Under the assumption of a parabolic velocity profile between the plates, one finds that the equation for the vorticity ω at the midplane is given by (2.3), but with $\lambda = 8\nu/e^2$. Based on this equation, one would expect exactly the same dynamics as in the case of an Ekman layer, only with different quantities determining the damping coefficient λ. However, in the immediate vicinity of the slit, diffusion in the horizontal plane cannot be assumed to be small, and the velocity profile between the plates will not be parabolic.

https://doi.org/10.1017/S0022112099004887 Published online by Cambridge University Press

This will have consequences for the initial instability, which can be expected to reflect three-dimensional aspects of the basic flow.

The different physical background of the rotating split-disk problem and the flow between parallel plates may give rise to different interpretations of the Reynolds number. The analogy between the two situations is most transparent if one interprets the length scale in the Reynolds number in both cases as the width of the shear layer. Assuming that (2.3) is valid, one can calculate this width from an equilibrium between $\lambda(\omega^* - \omega)$ and $\nu\nabla^2\omega$. Neglecting the curvature of the shear layer, one finds exponential functions on either side of the discontinuity in ω^*, decreasing on a length scale $d = (\nu/\lambda)^{1/2}$. In the case of a Stewartson layer this gives $d = E^{1/4}H$; for flow between parallel plates one finds $d = e/2\sqrt{2}$. Rabaud & Couder (1983) and Chomaz *et al.* (1988) used a Reynolds number defined as $a\Delta\Omega e/\nu$; this corresponds to our definition multiplied by a factor $4\sqrt{2}$. In reality, however, the validity of (2.3) for the flow between parallel plates is affected by the three-dimensional nature of the actual velocity field close to the slit. Rabaud & Couder (1983) gave an expression for the three-dimensional flow field if the circular curvature is neglected. A numerical evaluation of the velocity $\exp(-1)$-thickness in the midplane according to their solution gives $d \approx e/2.59$, slightly larger than, but close to the value following from (2.3). Note that a more rigid definition of the Reynolds number in which all scales are given by external parameters (such as the definition used by Rabaud & Couder (1983) and Chomaz *et al.* (1988), in which the fluid depth is used as the length scale) would be the preferred choice in one class of experiments, but it inevitably turns out to be unsuitable in the other. In § 4, we will show experimentally that our definition with the Stewartson-layer thickness as length scale is the most adequate for our experiments.

Comparing both types of experiments from a wider point of view, one may consider them as extreme examples of a generic class of split-disk problems in which the background angular velocity is allowed to vary. In our experiments, the background rotation is so fast that the flow should be described in terms of Ekman and Stewartson layers. In the case of Rabaud & Couder (1983) and Chomaz *et al.* (1988) the flow profile between the plates is determined by viscosity, and as long as the distance e between the plates is much smaller than estimates of the Ekman-layer thickness, background rotation is not an issue.

2.5. *Scaling law for vortex size in two-dimensional flows*

In order to estimate the number of vortices in the final state, Manin (1990) proposed a scaling argument for flows dominated by Ekman friction. In this argument, viscous diffusion is assumed to be negligible; it is shown by Dolzhanskiĭ *et al.* (1990) that this is a good approximation for strongly nonlinear flows. The flow can therefore be described by

$$\frac{\partial\omega}{\partial t} + \boldsymbol{v}\cdot\nabla\omega = -\lambda\omega + F, \tag{2.5}$$

where $F = \lambda\omega^*$ is considered explicitly as a forcing term. The argument relies on the existence of an inertial range in which energy cascades from small to large scales, characterized by a Kolmogorov spectrum $E(k) \sim \epsilon^{2/3}k^{-5/3}$, $E(k)$ being the spectral energy density, ϵ the cascading energy flux, and k the wavenumber. The main idea is that vortices grow in size until their turnover time $\tau_{\text{t.o.}}$ becomes comparable with the spin-down time $\tau = \lambda^{-1}$. This turnover time is expressed as $u^{-1}k^{-1}$, where u is to be interpreted as $E^{1/2}k^{1/2}$, that is, a velocity $u(k)$ typical of scale k (not a spectral velocity density). Making use of the Kolmogorov law, this gives $\tau_{\text{t.o.}} \sim \epsilon^{-1/3}k^{-2/3}$.

https://doi.org/10.1017/S0022112099004887 Published online by Cambridge University Press

Equating this with τ, one finds a minimal wavenumber $k_\lambda = \lambda^{3/2}\epsilon^{-1/2}$. Next, the cascading energy flux is found as follows. At some given large wavenumber k_0, energy is added to the system. In this regime, the forcing term has the same magnitude as the advective term, so $u_0^2 k_0^2 = F$. At the other end of the scale, dissipation takes place, so that $\epsilon \sim u^2/\tau \sim u^2/\tau_{\text{t.o.}} \sim u^3 k$. Since the flux of cascading energy is the same over the inertial range, this can also be written as $\epsilon \sim u_0^3 k_0$, or, expressed in terms of the forcing, $\epsilon \sim F^{3/2} k_0^{-2}$. With the expression for the minimal wavenumber, one arrives at $k_\lambda \sim k_0 (F/\lambda^2)^{-3/4}$. At this point, the terminology in Manin (1990) becomes somewhat confusing: the dimensionless parameter F/λ^2 is first called the Richardson number and further on the Reynolds number. However, F/λ^2 seems to be a parameter which is typical of (2.5), but different from both the Reynolds number and the Richardson number. In the case of an unstable shear layer in a split-disk configuration, F/λ^2 is proportional to $\Delta\Omega/\lambda$, which can be written as $Ro\, E^{-1/2}$. For fixed Ω and H this is indeed proportional to the Reynolds number as we use it in the present paper, so in that case the terminology used by Manin still applies. Thus, we may say that for constant depth, the number of vortices is proportional to $Re^{-3/4}$.

2.6. *The beta-effect and non-uniform depth*

In geophysical fluid dynamics, the atmospheric and oceanic flows are influenced by the latitudinal gradient in the background vorticity f, usually referred to as the Coriolis parameter. This gradient is due to the global variation of the normal component of the angular velocity Ω_e of the earth according to $f = 2\Omega_e \sin\alpha$, with α being the geographical latitude. Thus, part of the background vorticity of the Earth is released as relative vorticity as the fluid moves southward, and vice versa. Locally, the Coriolis parameter f can be approximated by a linear expansion in the geographical latitude, so $f = f_0 + \beta y$, with y being the local northward direction. According to this approximation, the change in relative vorticity per unit of time is $-\beta v_y$, where β is assumed to be uniform over the domain under consideration.

A similar effect is induced by a gradient in the depth of the fluid layer, since vortex tubes moving toward the deeper part are stretched and thus gain vorticity, and vice versa. For a layer of fluid with depth $H(r)$ depending only on the distance r from the rotation axis, the increase in relative vorticity per unit of time can be written as $\beta_{\text{top}} v_r$, with $\beta_{\text{top}} = 2\Omega H^{-1} \mathrm{d}H/\mathrm{d}r$. Apart from an opposite sign (caused by the radial direction being outward and the geophysical y-direction being toward the North Pole), this coincides with the β-effect in geophysics (see also Nezlin & Snezhkin 1993; van Heijst 1994). Including the β-effect, the vorticity equation becomes

$$\frac{\partial \omega}{\partial t} + \boldsymbol{v} \cdot \nabla \omega - \beta v_r = \lambda(\omega^* - \omega) + \nu \nabla^2 \omega. \tag{2.6}$$

The left-hand side can be written in a compact way as $\mathrm{D}Q/\mathrm{D}t$, where $\mathrm{D}/\mathrm{D}t$ is the total derivative and $Q = \omega - \beta r$ the potential vorticity. If the terms on the right-hand side are negligible, the potential vorticity is a conserved quantity for each fluid element.

2.7. *Linear stability theory*

Consider the stability of a circular shear layer in a rotating fluid with azimuthal velocity $V(r) = -\partial\psi_0/\partial r$, with $\psi_0(r)$ the stream function of the unperturbed basic flow. Niino & Misawa (1984) linearized (2.3) around the basic flow according to

$$\psi(r,\theta) = \psi_0(r) + \epsilon\widetilde{\psi}(r)\mathrm{e}^{\mathrm{i}k(r\theta - ct)} \tag{2.7}$$

https://doi.org/10.1017/S0022112099004887 Published online by Cambridge University Press

and evaluated the imaginary part of the complex phase velocity c; the flow becomes unstable if Im $c < 0$. Briefly summarized, they found that the flow becomes unstable above a critical Reynolds number for a specific wavenumber k. As the Reynolds number is increased, the range of wavenumbers for which the flow is unstable becomes wider, and the fastest growing unstable mode shifts to a larger wavenumber.

If the forcing profile is continuous, the viscous term can be shown to be much smaller than the Ekman damping term (Dolzhanskiĭ *et al.* 1990), and may be neglected in the stability analysis. As was pointed out by Niino & Misawa (1984), neglecting viscous diffusion is not acceptable in the case of a discontinuous shear forcing, since in that case a Stewartson layer is formed in which there is an equilibrium between viscous diffusion and Ekman pumping. However, in the experiments in the present paper the final shear layer becomes much wider than the initial Stewartson layer. Therefore, ignoring viscous diffusion may give an indication of the stability properties of the final, averaged shear layer. If the viscous term is dropped, one finds the Rayleigh stability equation for inviscid flows, generalized with a term to account for Ekman damping:

$$\widetilde{\psi}'' + \frac{1}{r}\widetilde{\psi}' + \left(\frac{V'' + V'/r - V/r^2}{V - c - \mathrm{i}\lambda k} - k^2\right)\widetilde{\psi} = 0. \tag{2.8}$$

In the same way as from the original Rayleigh equation, one can derive that in order to be unstable, the flow has to fulfil $V'' + V'/r - V/r^2 = 0$ somewhere in the domain.

The stability of the shear layer in the presence of a β-effect using this approximation has been studied by several authors, see Manin (1989) and references therein. Again, one may use an analogous stability analysis based on harmonic modes. By substituting (2.7) in (2.6), one finds that $V'' + V'/r - V/r^2 - \beta = 0$, which irrespective of the sign of β is a stronger constraint than $V'' + V'/r - V/r^2 = 0$. Although this result does not lead to clear-cut conclusions for small β, it is indicative of a stabilizing influence of the β-effect on the shear flow. More detailed information on the influence of a β-effect on the stability of two specific shear profiles was presented graphically by Manin (1989). The result for both cases is a decrease in the range of unstable wavenumbers, and a reduction of the growth rate of the unstable modes. Thus, we expect the β-effect to have a stabilizing effect on the shear flow, in the sense that the vortices remain smaller than on an f-plane.

In addition to these shear instabilities, there is a possibility of three-dimensional instabilities. In this respect, one is reminded of studies of the instability of freely evolving vortices in a rotating fluid (Kloosterziel & van Heijst 1990; Beckers & van Heijst 1998), to which the forced flow in the present paper bears a certain resemblance. Theoretical aspects of this subject were studied recently by Leblanc & Cambon (1997), who derived a generic criterion for three-dimensional instabilities in a rotating fluid. However, three-dimensional instabilities were never observed in our experiments.

3. Experimental set-up

The experiments were performed in a shallow layer of water in a rotating parabolic tank. An overview of the set-up is shown in figure 1. The shape of the parabolic tank corresponds to the free surface of a liquid rotating at $\Omega_0 = 7.53\,\mathrm{rad\,s^{-1}}$; this value will be referred to as the nominal angular velocity Ω_0. Having a central depth of 23 cm, the parabolic surface would fit in a cylinder with radius 28 cm and height 23 cm. A circular shear layer could be created by a differential rotation of the central part of the tank. This polar section has a radius $a = 10\,\mathrm{cm}$; the width of the slit

https://doi.org/10.1017/S0022112099004887 Published online by Cambridge University Press

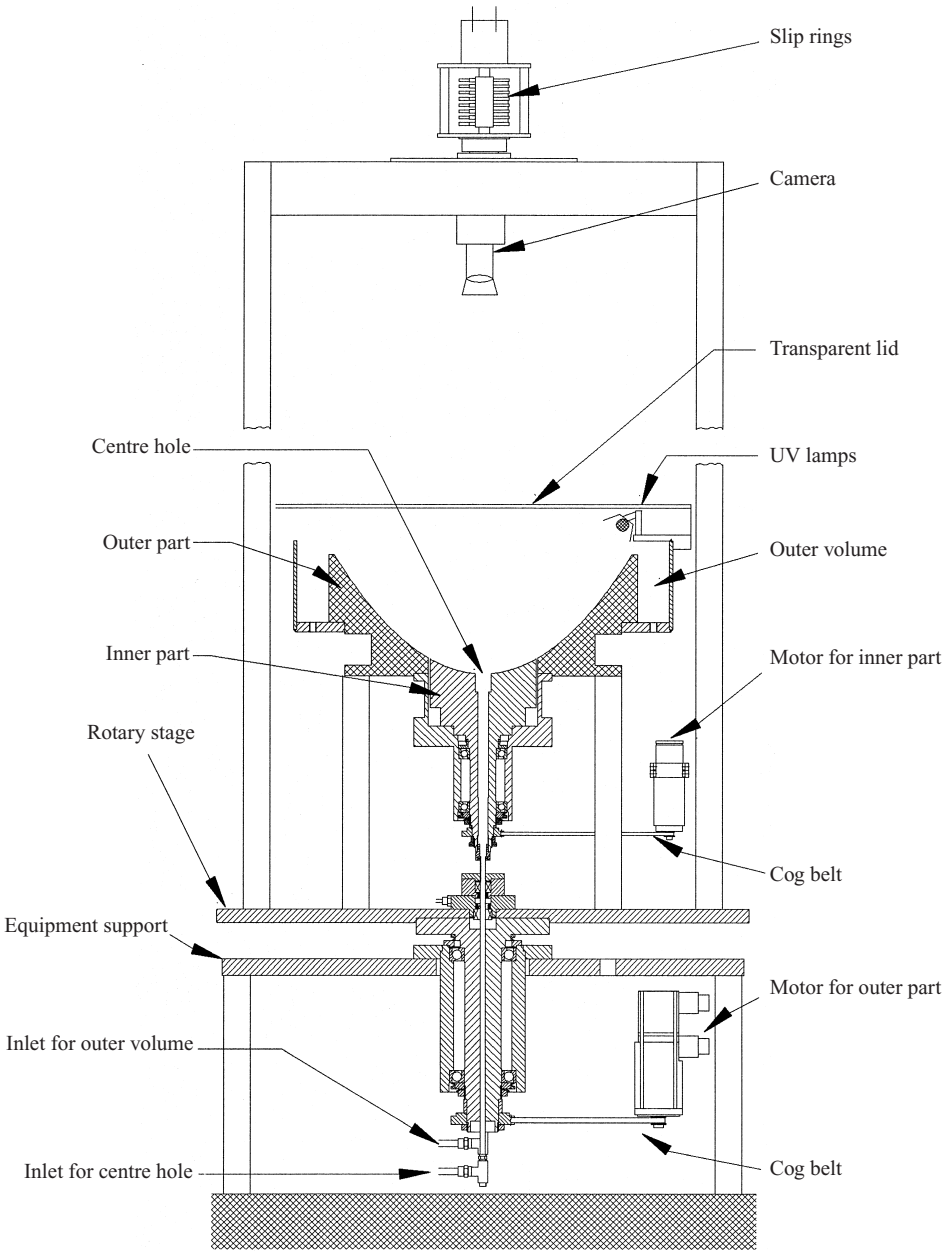


FIGURE 1. The experimental set-up.

between the inner disk and the main part of the tank is 0.3 mm. In the middle of the inner disk there is a hole with radius 1.5 cm. This hole is connected to a vertical tube outside the rotating system, so it was possible to measure the central depth of the fluid layer while the tank was rotating. A circulation system with controllable flow rate makes it possible to sustain a flow from the periphery of the paraboloid to the centre, or vice versa. Both the motors driving the main and the differential rotation are accurate to 0.1%. For the present study, the paraboloid has been covered

https://doi.org/10.1017/S0022112099004887 Published online by Cambridge University Press

with a flat transparent lid in order to eliminate possible friction with the air in the laboratory. The paraboloidal section is surveyed by a video camera mounted in the rotating frame and connected to the equipment in the laboratory via slip rings. The rotating fluid layer is illuminated by an ultraviolet light tube, mounted below the rigid lid. An ultraviolet filter was placed in front of the lens of the video camera, so that only fluorescent light is recorded.

The experiments were performed with a fluid depth varying between 5 and 60 mm. Even for the shallowest layer, this is much larger than the thickness of the Ekman layer, which is of the order of 0.3 mm. In most cases we used a depth of either 10, 20 or 40 mm, corresponding to values for the Ekman number of 1.3×10^{-3}, 3.3×10^{-4} and 8.3×10^{-5}, and spin-up times given by 3.6, 7.3 and 15 s, respectively. The angular velocity of the inner disk was chosen in the interval from -2.2 to $2.2\,\mathrm{rad\,s^{-1}}$, so the Rossby number had values between -0.29 and 0.29. Note that in this paper, we are using the vertical depth, not the depth perpendicular to the local sloping bottom of the parabolic vessel; the difference between these points of view is discussed in § 4.4. If the vertical depth is not uniform, such as in the case of a very fast inner rotation, we always refer to the depth at the edge of the inner disk.

The experiments with β-effect were performed at a background rotation different from the nominal angular velocity: $\Omega = 7.33\,\mathrm{rad\,s^{-1}}$ ($\beta < 0$) or $\Omega = 7.73\,\mathrm{rad\,s^{-1}}$ ($\beta > 0$). In both cases the depth at $r = a$ was equal to either 1 or 4 cm. In the geophysical situation, fluid moving away from either the North or the South Pole acquires cyclonic vorticity. Regardless of the rotation sense of the vessel, this corresponds to a layer of water that is shallow in the centre, and deep at the periphery. Thus, the case $\beta > 0$ corresponds to the situation around either of the poles, whereas the case $\beta < 0$ has no geophysical analogue. For convenience, we will adopt the terminology of the northern hemisphere, on which 'north' corresponds to shallow, and 'south' to deep.

In addition, we performed experiments in which a permanent flux $Q = 0.20\,\mathrm{l\,min^{-1}}$ was added at the centre and withdrawn from the periphery. In the absence of differential rotation, this condition leads to a steady state with an azimuthal interior flow, in which the entire flux is transported through an Ekman layer. One can derive from the properties of Ekman layers that this azimuthal velocity is given by $v_\theta(r) = -Q/\pi\delta r$, where δ represents the thickness of the Ekman layer. The method of creating an annular shear flow by a sink or source has been used earlier, see Trieling, Linssen & van Heijst (1997) and references therein. This azimuthal velocity field is accompanied by a depth gradient $\mathrm{d}h/\mathrm{d}r$ which we compensated for by taking a slightly higher background rotation. From geostrophic balance and centrifugal elevation we have $g\,\mathrm{d}h/\mathrm{d}r = 2\Omega v_\theta + (\Omega^2 - \Omega_0^2)r$; equating this to zero for $r = a$ gives an angular velocity of $7.81\,\mathrm{rad\,s^{-1}}$. The depth at $r = a$ can be calculated from the central depth measured in the absence of pumping, by compensating for the background rotation being slightly higher than Ω_0 and the change in depth that takes place when the pumping is turned on.

4. Experimental results

4.1. *Evolution of the shear layer*

Figure 2 presents an overview of the flow evolution in a typical experiment without β-effect. Before the start of the experiment, dyed water is pumped in through the central hole and spreads through the Ekman layer at the bottom. Immediately after the onset of the inner rotation ($t = 0$), the dye is advected towards the edge of

https://doi.org/10.1017/S0022112099004887 Published online by Cambridge University Press

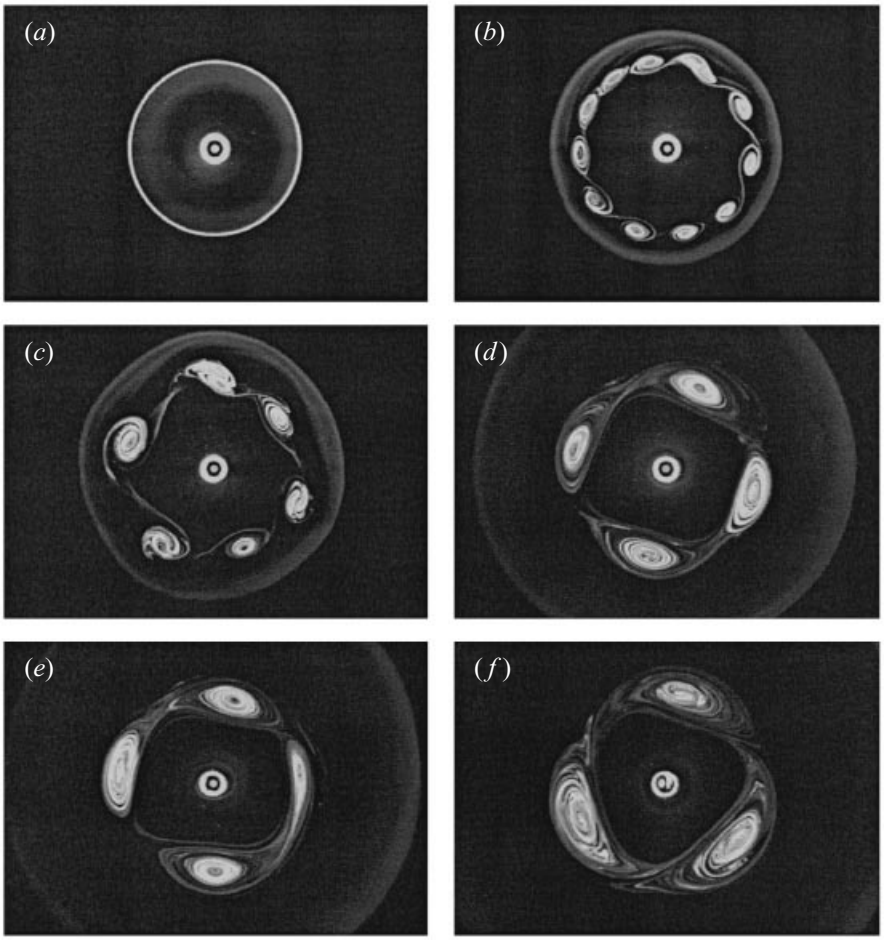


FIGURE 2. Evolution of an unstable shear layer to a mode three. Experimental parameters: $H = 2\,\mathrm{cm}$, $Re = 90$, $\Omega = \Omega_0$. The pictures (a–f) were taken at 0, 10, 16, 52, 70 and 112 s.

the inner disk, and the shear layer becomes visible as a concentrated circle of dye (figure 2a). The shear layer rolls up into a large number of vortices (figure 2b), which merge quickly into bigger ones (figures 2c and 2d). As the number of vortices decreases, however, the merging process becomes slower. In figure 2(d), we can see a configuration of four vortices that will undergo a transition into a mode with three vortices. Unlike the vortex mergers earlier on, this transition takes place gradually. The key factor in the transition mechanism is that one vortex is, or becomes, smaller than the rest. This small vortex moves slightly faster than the other vortices in the chain, and soon collides with the vortex in front of it. In the following interaction process the small vortex strips off a large part of the larger vortex, while the remainder is expelled as a new vortex, now becoming the smallest one in the chain. In figure 2(e), this small vortex can be seen at the right side. This collision process may be repeated many times. Every time, the smallest vortex becomes slightly weaker, until it eventually merges completely with the vortex in front of it. Thus, the transition takes place through a non-material disturbance that may travel around the vortex

https://doi.org/10.1017/S0022112099004887 Published online by Cambridge University Press

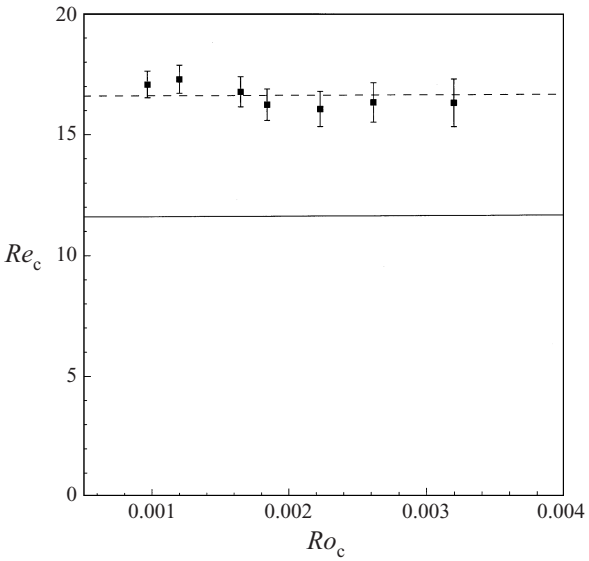


FIGURE 3. Reynolds number and Rossby number at the threshold of the instability. The measurements were taken at different depths; from left to right, $H = 60$, 40, 20, 15, 10, 7.5 and 5 mm. The dashed lines represent and the average of the critical Reynolds number of our measurements, the solid line the result of Niino & Misawa (1984).

chain many times. This mechanism guarantees that in the final state, all vortices have approximately the same size (figure 2*e*).

4.2. *The initial instability*

Figure 3 shows the Reynolds number versus the Rossby number at the threshold of the instability. Each of the data points corresponds to a certain depth. The quantity that was measured is the highest inner velocity $\Delta\Omega$ for which no wavy perturbations in the dyed fluid were observed. The measurements confirm the result of Niino & Misawa about the Reynolds number being the determining factor for the instability, but the critical value we find ($Re_c = 16.6 \pm 0.6$) is higher than that of Niino & Misawa (theory $Re_c = 11.6$; experiment $Re_c = 11.7 \pm 0.6$). A quantitative explanation for this difference is still lacking, but in § 4.4 it is shown that part of the discrepancy may be explained by the curvature of the vessel.

4.3. *Properties of the final state*

In figure 4, a selection of different symmetry modes found in experiments with $H =$ 2 cm is shown. The pictures in this figure were taken at least 10 minutes after the onset of the inner rotation; by this time any transient phenomena had disappeared. After the settling time, we slowly pumped in a small amount of dyed fluid. This dye is advected outwards through the Ekman layer, and is partially sucked up in the shear zone. Figure 4 demonstrates a number of qualitative features. The first is the symmetry of the vortex chain. In particular, the modes with $n \geqslant 4$ turn out to be perfectly symmetric and steady, a further indication of a distribution mechanism between the vortices. In the experiments with $n = 3$ and $n = 2$, the flow is no longer stationary. In the case $n = 3$, there were slight oscillations around a symmetric configuration; the vortices never seemed to obtain quite the same size, and the triangular ring of dye forming the inner boundary of the vortices showed a periodic deformation. In the

https://doi.org/10.1017/S0022112099004887 Published online by Cambridge University Press

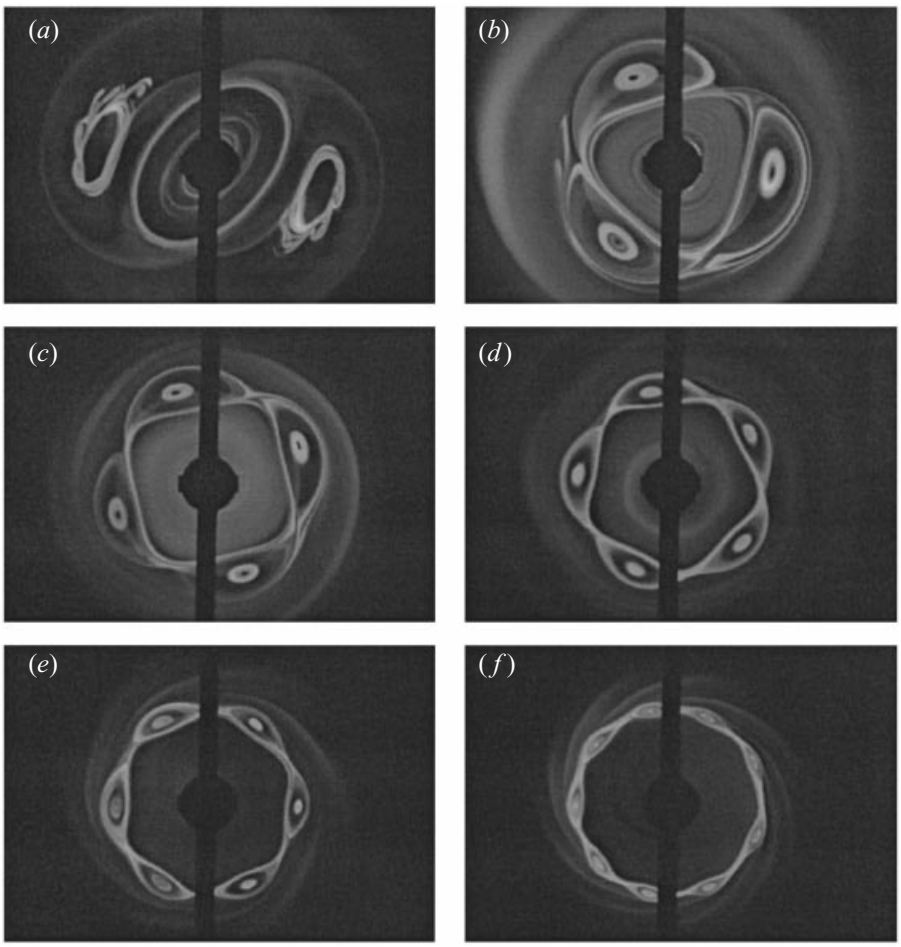


FIGURE 4. Stationary vortex distributions for $\Omega = \Omega_0$, cyclonic inner rotation, and $H = 2$ cm. From mode number 2 to mode number 9, the Reynolds number is 180, 88, 44, 28, 24 and 20 (*a–f*).

case $n = 2$, there was a periodic formation and decay of small inner vortices, showing up in figure 4(*a*) as undulations in the rings of dye around the vortex cores. These oscillations also appear for higher mode numbers if the depth is decreased. In some cases, a stable asymmetric flow appears: just above the critical value for $n = 2$, the two anticyclonic vortices may have a different shape, and only one of them may show oscillations whereas the other one is steady (see figure 5). This asymmetry disappears if the speed of the inner disk is increased, and returns if the inner disk is slowed down again. Figure 6 shows an experiment with an anticyclonic inner rotation. In that case the dye distribution becomes more diffuse than for cyclonic inner rotation, and the picture has the appearance of a photographic negative of the corresponding mode three in figure 4. At moderate values for the inner rotation, there seems to be little difference between cyclonic and anticyclonic motion.

Another observation in figure 4 is that the dye is concentrated along the periphery of the vortices and in the eye-like rings in the vortex centres. Seen from above, these rings always touch the slit. Figure 7 shows a close-up of a ring taken with a camera looking down obliquely at the shear layer, shortly after a small amount of dye has

https://doi.org/10.1017/S0022112099004887 Published online by Cambridge University Press

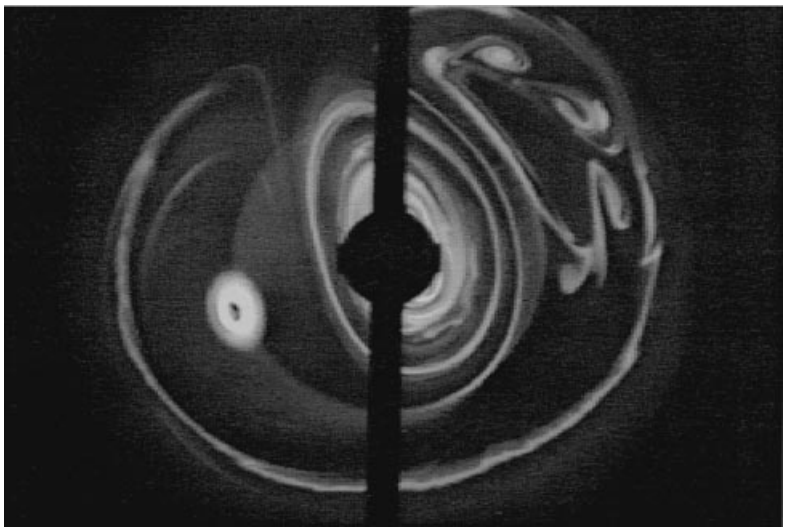


FIGURE 5. Asymmetric final state for $\Omega = \Omega_0$, $H = 4\,\mathrm{cm}$, and $\Delta\Omega = 0.73\,\mathrm{rad\,s^{-1}}$. The asymmetry is persistent; one of the satellites is a smooth vortex, whereas the other one is a cluster of smaller structures that are continuously being formed and destroyed.

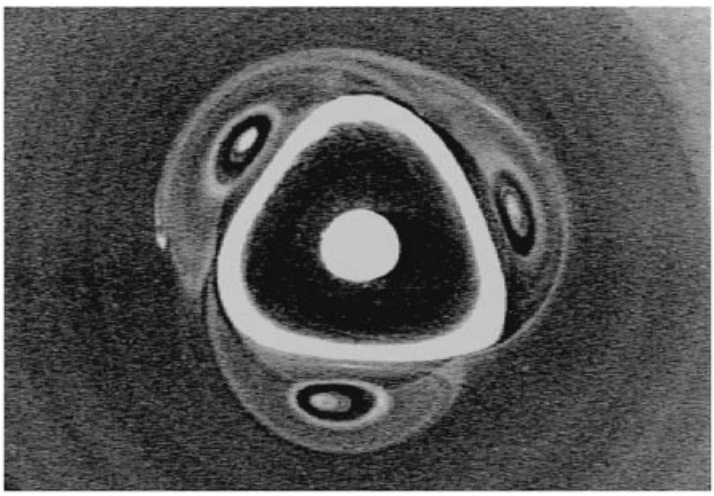


FIGURE 6. Stationary mode three for $\Omega = \Omega_0$, anticyclonic inner rotation, and $H = 2\,\mathrm{cm}$. The Reynolds number is -100.

been added through the central hole. Dye is visible at the edge of the vortex and in the eye-like ring, which now appears as a half-torus. In the course of the experiment, this half-torus expands upward, outward as well as inward, finally resulting in a dyed volume with a cylindrical shape. In a top view, the ring gradually becomes thicker, until the dark part of the eye disappears and a more or less uniformly dyed patch remains. Thus, the following qualitative picture appears. As a property of the two-dimensional vorticity equation, the centres of the vortices are located slightly outside $r = a$, the radial position of the slit. Because of the singular negative vorticity of the differentially rotating bottom, dye is sucked up by the shear layer. Apparently, the dye appears only at places where there is no velocity component across the slit. This effect

https://doi.org/10.1017/S0022112099004887 Published online by Cambridge University Press

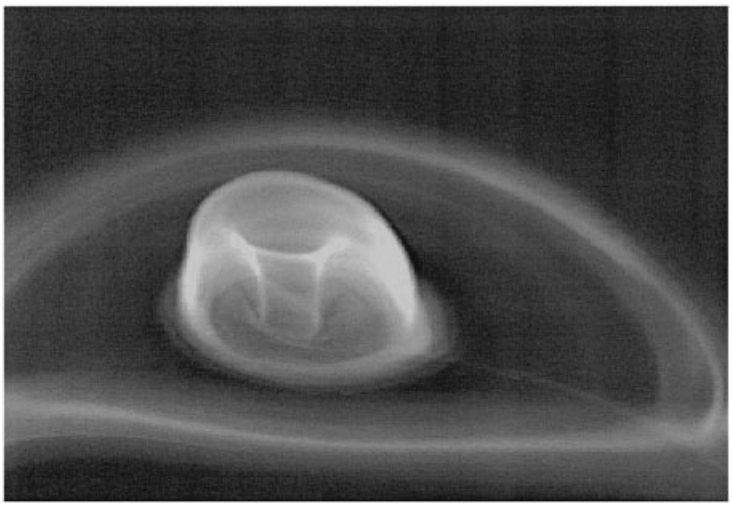


FIGURE 7. Close-up of a steady vortex, made with a camera in a tilted position looking down onto the vortex at an angle of approximately 45° with the vertical. Experimental parameters: depth 4 cm, $\Omega = 7.53\,\mathrm{rad\,s^{-1}}$, $\Delta\Omega = 0.58\,\mathrm{rad\,s^{-1}}$. The flow field is of mode three. The slit is visible as a faint curve from the lower right corner of the picture to the centre of the vortex.

lies outside the scope of linear Ekman-layer theory; the strong velocity gradients in the horizontal plane at the position of the slit in combination with cross-flow over the slit provides a situation where the advective term cannot possibly be small. In any case, the dye is observed to leave the Ekman layer only between the vortices (leading to contour lines around the vortices), and at one point inside each vortex (leading to the dyed rings). As in a Stewartson layer, the dye has to move down again in a local circulatory motion. As a consequence, the central rings are at first very thin, but gradually grow into a torus and later on into a filled column. If the experiment is repeated with anticyclonic inner rotation, the vortices are cyclonic, and the secondary flow is reversed. The vortices then expel dye, and their centres become visible as dark rings against a dyed background (see figure 6).

Figure 8 shows the number of modes in the final state versus the Reynolds number. For very small Reynolds numbers, the initial shear layer is stable. Every experiment leading to an unstable shear layer was carried out at least three times; the experiments that yielded many vortices even four or five times. The data show that the number of vortices is highest just beyond the critical Reynolds number, and decreases to two as the Reynolds number is increased. This observation is in agreement with the scaling law of Manin (1990), according to which the size of vortices should be proportional to $Re^{3/4}$. A best fit of the corresponding $Re^{-3/4}$-dependence on the number of vortices has been included in figure 8, and the agreement with the data appears to be good.

Furthermore, the figure shows a certain overlap between the plateaux corresponding to the different mode numbers. Apparently, an experiment with a certain combination of parameters may have different stable solutions, an observation also made by Rabaud & Couder (1983) and Niino & Misawa (1984). In fact, there is more hysteresis in the vortex chain than is apparent from figure 8. If the inner rotation is increased or decreased slowly starting from a certain mode number, the flow may remain longer in that mode than the horizontal plateaux in figure 8 suggest. The horizontal parts do not indicate the stability boundaries of the modes concerned, but

https://doi.org/10.1017/S0022112099004887 Published online by Cambridge University Press

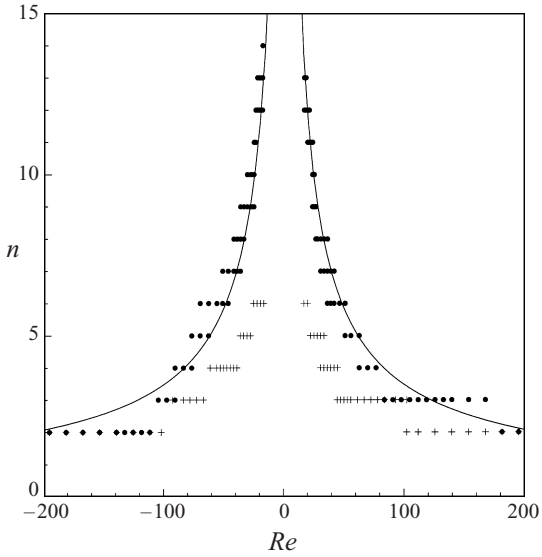


FIGURE 8. Number of modes versus Reynolds number for $H = 1\,\mathrm{cm}$ (dots) and for $H = 4\,\mathrm{cm}$ (crosses); $\Omega = \Omega_0 = 7.53\,\mathrm{rad\,s^{-1}}$ ($\beta = 0$).

rather the most likely outcome of the experiment as the inner disk is set into rotation instantaneously.

For a given Reynolds number, the number of vortices decreases strongly with increasing depth of the fluid layer. Since the depth enters the vorticity equation through the Ekman number, this phenomenon has to be related to the amount of damping of the two-dimensional flow above the Ekman layers. According to the measurements, a weaker damping increases the extent to which merging in the vortex chain takes place. Oppositely, at smaller depths the number of vortices becomes larger. In experiments with a fluid depth of 5 mm, we observed as many as 20 vortices.

4.4. *Axial alignment of the vortices*

When the bottom of a fluid layer has a local inclination with respect to $\boldsymbol{\Omega}$ (such as in the experiments in the present paper, or at any location on the Earth except for the Poles), two viewpoints can be taken.

The first is to take a Cartesian coordinate system with the x- and y-axes in the local bottom plane and the z-axis in the normal direction. One then decomposes the angular velocity along these axes, and assumes that the velocity field is uniform over the fluid depth, measured in the z-direction. In this way it is easier to impose boundary conditions if calculations are made, but one abandons the Taylor–Proudman theorem for the weaker shallow-water assumption.

The second viewpoint is to use a coordinate system with the z-axis in the direction of $\boldsymbol{\Omega}$. The observation we would like to report here is that our experiments seem to favour this view; dye visualizations performed with a fluid depth of 4 cm indicate that vortical structures are aligned with $\boldsymbol{\Omega}$, not with the local normal to the bottom plane. For a very shallow fluid layer and for small Rossby number, these two viewpoints lead to the same result with respect to the β-effect (or, in fact, any higher-order topography/background variation). Consider a layer of fluid with a depth that is uniform in the direction parallel to $\boldsymbol{\Omega}$, then there is obviously no β-effect according to the second viewpoint. In the first viewpoint, one finds two terms cancelling one

https://doi.org/10.1017/S0022112099004887 Published online by Cambridge University Press

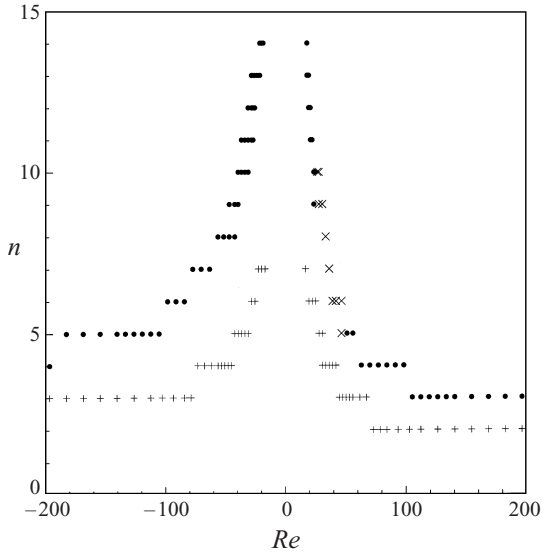


FIGURE 9. As in figure 8, but for $\Omega = 7.33\,\mathrm{rad\,s^{-1}}$ ($\beta < 0$).

another: minus the gradient of the background vorticity $2\Omega\cos\theta$, and $2\Omega/H$ times the gradient of the local depth H, which can be written as $H_0\cos\theta$.

However, in the second picture the inclination also plays a role, since it affects the Ekman pumping in the vertical direction. According to a calculation given by Pedlosky (1987), the Ekman pumping velocity for a shallow layer of fluid with uniform inclination θ is $\frac{1}{2}(\nu/\Omega)^{1/2}(\cos\theta)^{-1/2}(\omega-\omega^*)$ in the normal direction, which corresponds to a pumping velocity $\frac{1}{2}(\nu/\Omega)^{1/2}(\cos\theta)^{-3/2}(\omega-\omega^*)$ in the vertical direction. This means an increase of the Ekman pumping rate by a factor $\cos^{-3/2}\theta$ with respect to a flat bottom, and an increase of the Stewartson-layer thickness by a factor $\cos^{-3/4}\theta$. In our case, with $\theta = 30^\circ$ at the radial position of the slit, this factor is 1.11. If we correct the critical Reynolds number found by Niino & Misawa (1984) with this factor, we arrive at $Re_c = 12.9$, which is closer to our measurements than the value for a horizontal fluid layer. However, if the boundary is curved, the theory cannot be applied, since for a general vorticity distribution it would lead to an imbalance between fluid being pumped into and out of the Ekman layer. Without detailed knowledge about the structure of the velocity field in three dimensions, the influence of the parabolic curvature on Ekman suction can be discussed at most qualitatively.

4.5. *Influence of the β-effect*

The introduction of a β-effect affects the mode number as well as the stability of the vortex chain. Figures 9 and 10 show the mode number versus the Rossby number for a background angular velocity of 7.33 and $7.73\,\mathrm{rad\,s^{-1}}$. In general, these graphs have the same appearance as in figure 8. For small absolute values of the Reynolds number, the shear layer is still very thin, and therefore affected little by the β-effect. For higher values, the β-effect becomes noticeable. On the left side of figure 9 and on the right side of figure 10, we can see the stabilizing influence of the β-plane expected from instability theory. However, on the opposite sides of these graphs, the effect is not observed. On the contrary, in a certain range of values for the Reynolds number, the vortex chain is unsteady; vortices always keep merging and

https://doi.org/10.1017/S0022112099004887 Published online by Cambridge University Press

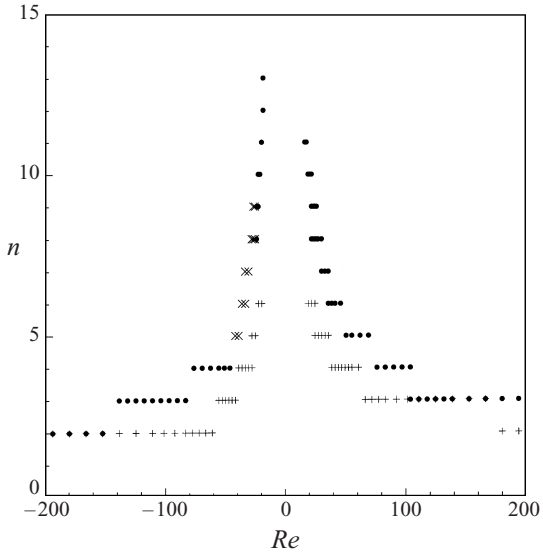


FIGURE 10. As in figure 8, but for $\Omega = 7.73\,\mathrm{rad\,s^{-1}}$ ($\beta > 0$).

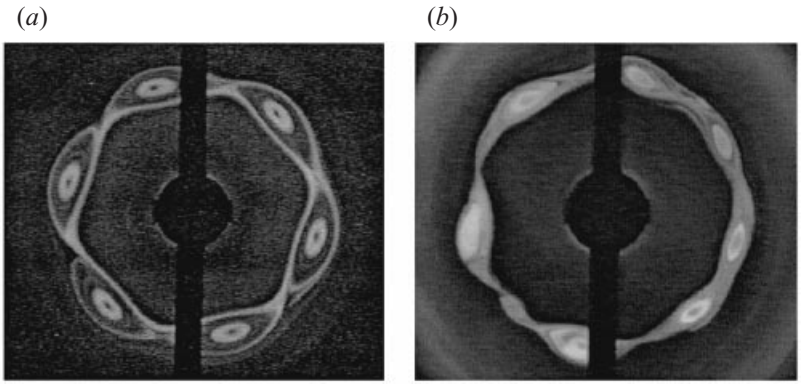


FIGURE 11. (*a*) Steady and (*b*) unsteady vortex distribution for a cyclonic inner rotation for $\Omega = 7.73\,\mathrm{rad\,s^{-1}}$ ($\beta > 0$) and $\Omega = 7.33\,\mathrm{rad\,s^{-1}}$ ($\beta < 0$), respectively. The depth at the radial position of the central disk is 1 cm.

being formed. In figures 9 and 10, the average number of vortices for such cases has been represented by separate symbols. A visualization of an unsteady vortex chain showing the asymmetry connected with the instability is given in figure 11. The instability occurs only for anticyclonic vortices in the $7.33\,\mathrm{rad\,s^{-1}}$ experiment and for cyclonic vortices in the $7.73\,\mathrm{rad\,s^{-1}}$ experiment, that is, only for vortices travelling in the 'westward' direction. As mentioned, for the inner rotation sense for which the instability does not occur, the number of vortices is higher than in the corresponding experiments without β-effect. This difference may also be related to the concavity of the region enclosed by the vortex chain. More detailed insight into this matter is provided by the numerical simulations.

https://doi.org/10.1017/S0022112099004887 Published online by Cambridge University Press

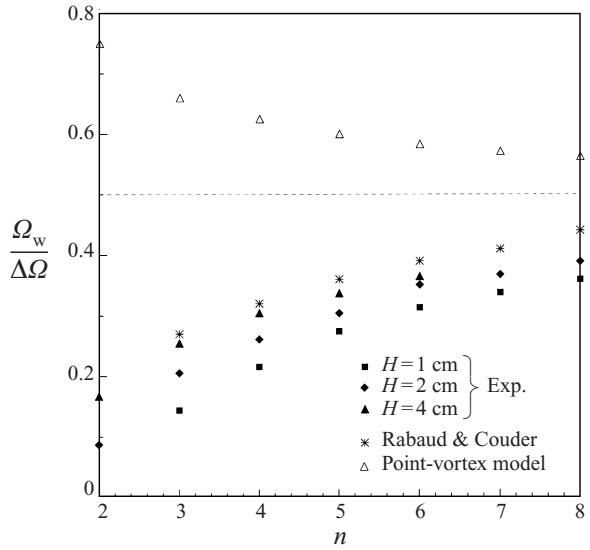


FIGURE 12. Comparison of the angular velocity of the vortex chain according to the point-vortex model with experimental data.

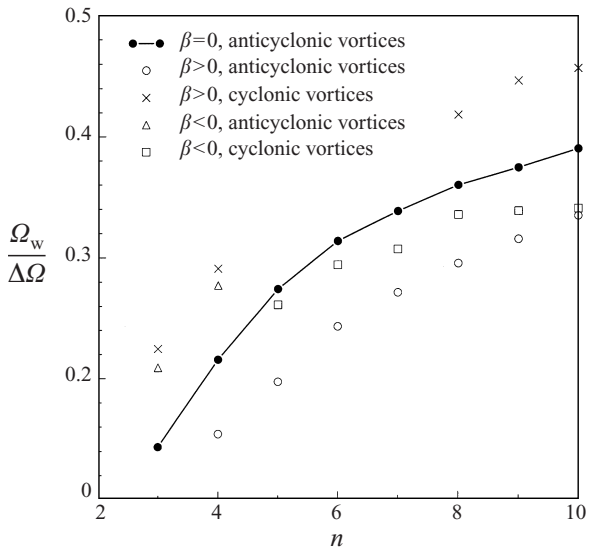


FIGURE 13. Angular velocity of the vortex chain with and without β-effect. The background angular velocity is given for $\beta < 0$, $\beta = 0$ and $\beta > 0$ by 7.33, 7.53 and 7.73 rad s^{-1}, respectively. The depth above the slit is 1 cm.

4.6. *Angular velocity of the vortices*

Next, consider the angular velocity of the vortices around the centre of the tank. Since the angular velocity at the bottom jumps from $\Delta\Omega$ to 0 at the edge of the inner disk, one would expect that the angular velocity of the vortices is close to $\frac{1}{2}\Delta\Omega$. However, figure 12 shows that large vortices move more slowly than this estimate, a result also found by Rabaud & Couder (1983).

As a first attempt to explain this discrepancy, one may represent both the rotating

https://doi.org/10.1017/S0022112099004887 Published online by Cambridge University Press

inner region and the vortices of the chain by point vortices. Denoting the circulation of the inner region by Γ, one finds that the motion of the chain vortices is purely azimuthal, with an angular velocity given by

$$\Omega_{\mathrm{w}} = \frac{\Gamma}{2\pi a^2}\frac{n+1}{2n}, \tag{4.1}$$

where n is the number of chain vortices. Figure 12 shows that this result is in poor agreement with the observed values. According to (4.1), the angular velocity of the vortex chain, scaled with $\Delta\Omega = \Gamma/2\pi a^2$, becomes higher if the number of vortices decreases; each vortex does not 'feel' its own vorticity, and the fewer vortices there are, the larger is the net vorticity of opposite sign contained by the other vortices. However, according to our measurements and those of Rabaud & Couder (1983) in a soap film, the scaled angular velocity actually decreases with the number of vortices. Further analysis indicates that this discrepancy is caused by the advection of vorticity to large radii: the central vortex is weakened, since part of its vorticity is transported outside the vortex chain where it does not contribute to the angular velocity of the vortices.

Figure 13 also includes measurements with β-effect. First, consider experiments with $\beta > 0$. In this case, cyclonic vortices are seen to move faster, whereas anticyclonic vortices move more slowly than in corresponding experiments with $\beta = 0$. This effect is caused by a transformation from potential vorticity to relative vorticity. Due to the circulation inside the vortices, a small excess vorticity of positive sign builds up on the outer side of the vortices, whereas negative vorticity builds up on the inner side. This results in a weak dipolar vorticity distribution overlying the vortices, leading to a more strongly anticyclonic, or less strongly cyclonic motion of the vortices around the centre. For $\beta < 0$, according to a similar argument the vortices get a velocity component in the cyclonic direction, as can be observed in figure 13.

4.7. *Influence of pumping*

The shear layer appears to be influenced strongly by even a small flux added or withdrawn at the centre. Figure 14 shows the number of vortices versus the Reynolds number for a fixed volume flux Q flowing in the fluid layer from the centre toward the periphery. For $Re < 0$, the inner rotation has the same sense as the azimuthal flow induced by the pumping. Since the shear induced by the two forcing mechanisms adds up, the vortices become elongated, and appear to be less coherent than without pumping. Because of their azimuthal extent, the vortices interact more easily, so their final number turns out to be somewhat smaller. On the other hand, for $Re > 0$ the direction of the inner rotation is opposite to pumping-induced shear flow, and for a certain combination of parameters the vortices come to a complete standstill in the system rotating with angular velocity Ω. In this case the vortices are stabilized, and we find more of them than without pumping. Figure 15 shows a visualization of two vortex chains with opposite inner rotation sense. One can see that the adverse shear leads to a pattern in which the vortices are more distinctly separated.

5. Numerical method

The evolution of an unstable shear layer, as discussed in the previous Sections, is highly complicated, both because of the parabolic geometry and because of three-dimensional features such as the structure of the Ekman layer. In this paper, we do not aim at a numerical representation of these effects; instead, we consider a two-

https://doi.org/10.1017/S0022112099004887 Published online by Cambridge University Press

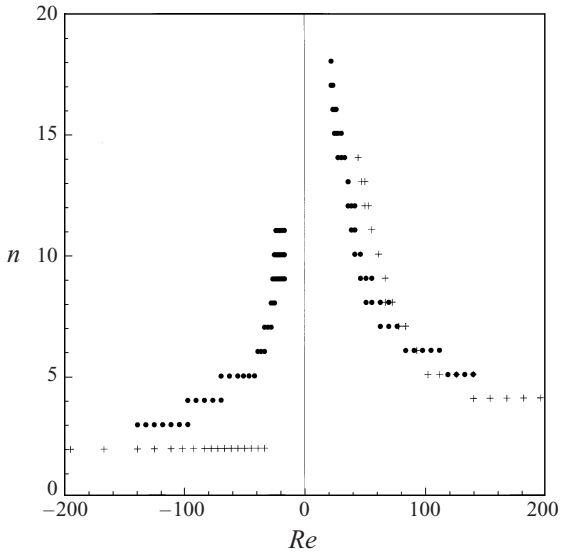


FIGURE 14. As in figure 8, but for pumping with $Q = 0.20\,\mathrm{l\,min^{-1}}$ and $\Omega = 7.81\,\mathrm{rad\,s^{-1}}$.

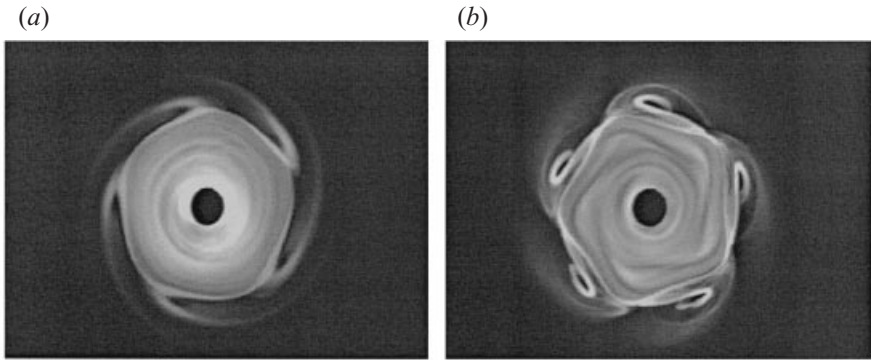


FIGURE 15. Visualization of vortex chains in the presence of pumping ($Q = 0.20\,\mathrm{l\,min^{-1}}$, $\Omega = 7.81\,\mathrm{rad\,s^{-1}}$) for $Re = -42$ (*a*) and $Re = 110$ (*b*).

dimensional model with a spectral code. This is not only easier from a computational point of view, but also provides insight into the extent to which the experimental observations are captured by the simplified equations.

We solved (2.6) in the vorticity–stream function formulation, given in polar coordinates (r, θ) by

$$\frac{\partial \omega}{\partial t} + J(\omega, \psi) - \frac{\beta}{r}\frac{\partial \psi}{\partial \theta} = \lambda(\omega^* - \omega) + \nu \nabla^2 \omega \tag{5.1}$$

in combination with the Poisson equation

$$\nabla^2 \psi = -\omega. \tag{5.2}$$

In these equations we have introduced the stream function

$$\nabla \psi \times \hat{\boldsymbol{e}}_z = \boldsymbol{v} \tag{5.3}$$

https://doi.org/10.1017/S0022112099004887 Published online by Cambridge University Press

and the Jacobian $J(f,g)$

$$J(f,g) \equiv \frac{1}{r}\left(\frac{\partial f}{\partial r}\frac{\partial g}{\partial \theta} - \frac{\partial g}{\partial r}\frac{\partial f}{\partial \theta}\right). \tag{5.4}$$

In the experiments, the slit width between the inner disk and the outer part is so small that the forcing can be considered as discontinuous. In the numerical simulations we have to allow for a finite width of the shear forcing. Expressed in terms of the azimuthal velocity v_θ^*, we model the forcing by

$$v_\theta^* = \tfrac{1}{2}\Delta\Omega r(-\tanh[(r-a)/c]+1) + \Omega' r, \tag{5.5}$$

where a is the radial position of the shear layer, and c the width of the shear. The value of c was chosen to be approximately the same as the thickness $E^{1/4}H$ of the Stewartson layer in the stable linear case. Since in reality the shear layer is nonlinear and develops into vortices with a much larger horizontal extent than the original Stewartson layer, we believe that no substantial errors are introduced by the non-zero value of c. The primed quantity Ω' is an *a priori* estimate of the angular velocity of the final vortex pattern based on the data of Rabaud & Couder. This offset angular velocity makes it somewhat easier to follow a single vortex, but has no further consequence for the outcome of the computation.

Equations (5.1) and (5.2) are solved in an annular geometry with inner radius r^- and outer radius r^+, by means of a fully dealiased pseudo-spectral code using a Fourier expansion in the azimuthal direction and an expansion in Chebyshev polynomials in the radial direction, according to

$$\omega(r,\theta,t) = \sum_{m=0}^{M}\sum_{n=-N/2}^{N/2-1} \omega_{mn}(t)T_m(\xi)\mathrm{e}^{\mathrm{i}n\theta}, \tag{5.6}$$

where ξ is a radial coordinate scaled to the interval $[-1;1]$ on which the Chebyshev polynomials are defined. The time evolution of the coefficients $\omega_{mn}(t)$ is followed in mode space by means of an implicit third-order Stiffly–Stable scheme, with the nonlinear term $J(\omega,\psi)$ being evaluated in configuration space. At each time step we thus have to solve the Poisson equation for ψ, and a Helmholtz equation for the vorticity. In the simulations presented here we have chosen free-slip boundary conditions, since this gives the most realistic approximation to the experimental situation, in which there is no inner wall, and the outer wall is far away from the shear layer. The boundary condition for ω is

$$\left.\frac{\partial \omega}{\partial r}\right|_{r=r^\pm} = 0; \tag{5.7}$$

note that as a consequence of (5.7), vorticity cannot leave the system by diffusion through the boundary. The boundary conditions for ψ depend on the Fourier mode number being zero or not, and can be expressed as

$$\psi_n(r^\pm) = 0 \quad (n \neq 0); \quad \left.\frac{\partial \psi_0}{\partial r}\right|_{r=r^\pm} = -\frac{r^\pm \omega_0(r^\pm)}{2}. \tag{5.8}$$

For further details on the numerical method, see Coutsias *et al.* (1994), Nielsen (1993), and Coutsias & Lynov (1991). In all the simulations presented below we have chosen $M = N = 256$, $r^- = 0.5$ CU, $r^+ = 2.5$ CU, $a = 1.5$ CU, $\Omega_0 = 7.53\,\mathrm{s}^{-1}$, $H = 0.15$ CU, $e = 0.03$ CU and $\nu = 2.25 \times 10^{-4}$ CU$^2\,\mathrm{s}^{-1}$, where CU (Computer Unit) is a length

https://doi.org/10.1017/S0022112099004887 Published online by Cambridge University Press

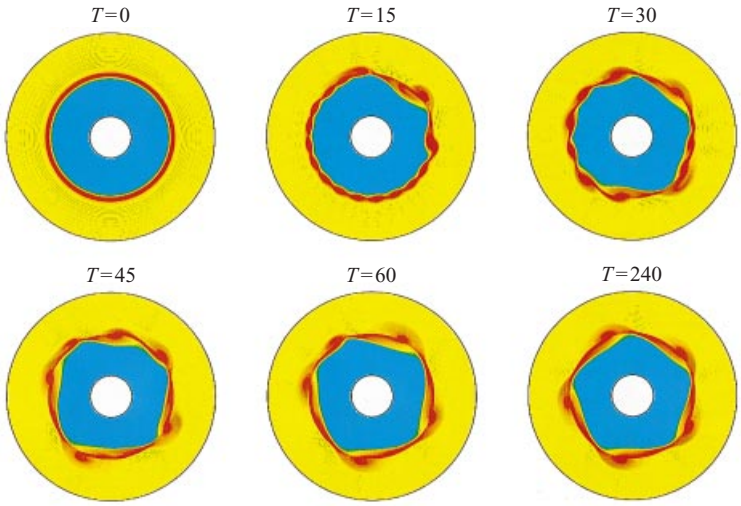


FIGURE 16. Vorticity distribution showing the formation of a mode 5. Blue corresponds to a negative vorticity, red to a positive vorticity, yellow to zero. Parameters: $\beta = 0$, $Re = 29.3$.

scale used in the computation. The radial position of the shear zone in the experiment was $a = 10\,\mathrm{cm}$, so all lengths are mapped such that $0.15\ \mathrm{CU} = 1\,\mathrm{cm}$; the time in the computer simulations is measured in seconds. Having chosen the parameters for the forcing term in (5.5), and thereby determined the Reynolds number, we initiated the computation with the basic flow, which is the solution of (2.6) with the left-hand side equal to zero. In order to trigger the instabilities, we added a small noise contribution localized at the shear zone. A numerical estimate of the width of the shear layer in the initial condition has been used as the length scale d in the Reynolds number.

Note further that (2.6) is invariant to the simultaneous reversal of θ, v_θ, ω and β, so that no new solutions are found if the signs of both ω^* and β are reversed. For this reason we only performed simulations with anticyclonic inner rotation.

6. Numerical results

In figure 16 we show the formation of a mode 5 evolving from the axisymmetric initial condition without β-effect. Since the Reynolds number is low the evolution is quite smooth. In order to clarify the dynamics for this evolution we have shown in figure 17 the spectrum of the enstrophy

$$Z(t) = \tfrac{1}{2}\int \omega^2 \mathrm{d}A \tag{6.1}$$

with A being the entire domain. By substituting the expansion

$$\omega(r,\theta,t) = \sum_{n=-\infty}^{\infty} \omega_n(r,t)\mathrm{e}^{\mathrm{i}n\theta} \tag{6.2}$$

in this definition, one finds after integration over θ that

$$Z(t) = \tfrac{1}{2}\sum_{n=-\infty}^{\infty}\int |\omega_n^2|(r,t)\,2\pi r\mathrm{d}r = \tfrac{1}{2}\int \omega_0^2(r,t)2\pi r\mathrm{d}r + \sum_{n=1}^{\infty}\int |\omega_n^2|(r,t)2\pi r\mathrm{d}r \tag{6.3}$$

https://doi.org/10.1017/S0022112099004887 Published online by Cambridge University Press

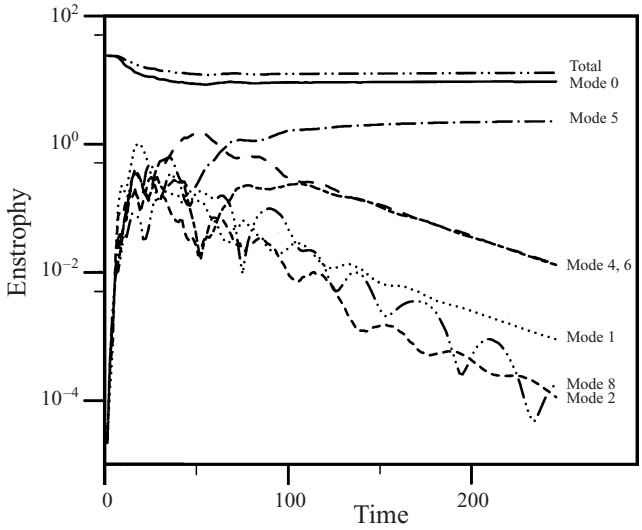


FIGURE 17. Enstrophy spectrum for the simulation of figure 16.

so the enstrophy may be interpreted as a sum over different modes. We use the expansion of the enstrophy to quantify the strengths of the different modes.

At $t = 0$, nearly all the enstrophy is in the zero mode, while all other azimuthal modes contain only the initial noise contributions. The subsequent evolution can be divided into three stages. First, during a short time, the unstable modes grow exponentially. Then, approximately at $t = 15$ the amplitudes have become so large that the advective term becomes dominant and all modes start to interact. Finally, after $t = 100$, mode 5 stabilizes itself at a well-defined enstrophy level, thereby eliminating all modes that are not a multiple of five. Thus, one may say that the forcing term in (5.5) is feeding enstrophy to the zero mode, the nonlinear term redistributes it to mode 5 and its higher harmonics, and from these modes enstrophy is removed by viscosity and Ekman damping.

In figure 18 we show the onset of the instability where the flow bifurcates from the axisymmetric state. The symbols indicate the saturated level of the maximal radial velocity squared, max v_r^2, as a function of the Reynolds number for three values of β. For Re smaller than a well-defined critical value $Re_c(\beta)$, all azimuthal modes die out, resulting in an unperturbed state. For Re slightly above Re_c, the squared amplitudes saturate at a level which grows linearly with Re, characterizing a supercritical bifurcation. Using linear extrapolation based on the two lowest non-zero data points, we find $Re_c(\beta = 0) = 14.5$, $Re_c(\beta = 3.012) = 14.8$ and $Re_c(\beta = -3.012) = 15.0$. From the spectrum we observe further that the first mode which becomes unstable is 13 for $\beta = 0$, and 14 for $\beta = \pm 3.012$. Including the β-term thus makes the basic flow slightly more stable as anticipated in § 2.7.

Figure 19 shows the observed number of modes versus the Reynolds number together with the experimentally obtained data of figure 8. Each numerical data point corresponds to a stable configuration of a numerical run. In general, there is good agreement between the experimental and numerical results. The computer simulations tend to produce a lower mode number than seen in the experiment for the same Reynolds number, but in view of the simple model for the Ekman pumping

https://doi.org/10.1017/S0022112099004887 Published online by Cambridge University Press

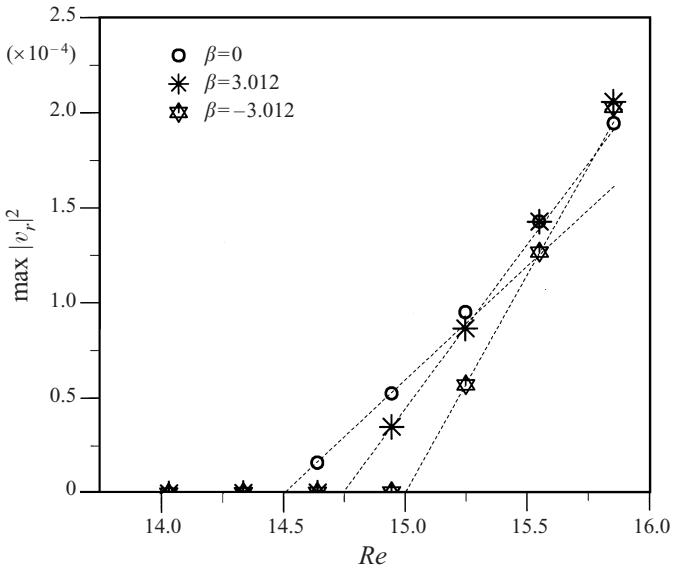


FIGURE 18. Saturated level of the maximal radial velocity squared as a function of the Reynolds number for $\beta = 0$, $\beta = 3.012$ and $\beta = -3.012$. The dotted lines are extrapolations based on the two lowest non-zero data points. The critical Reynolds numbers found in this way are $Re_c(\beta = 0) = 14.5$, $Re_c(\beta = 3.012) = 14.8$ and $Re_c(\beta = -3.012) = 15.0$.

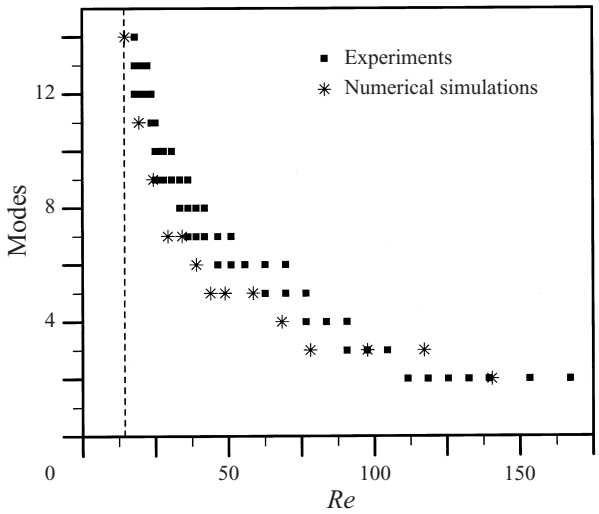


FIGURE 19. Comparison of the experimental and numerical mode number for $H = 1$ cm and $\beta = 0$.

mechanism and the fact that the parabolic curvature is not taken into account, these results are quite acceptable.

The influence of the β-term can be seen in figure 20, which shows the final states of nine numerical runs with different Reynolds numbers and values for β. Inclusion of a β-effect stabilizes the flow, and we observe a larger number of vortices for the same Reynolds number. Another observation is that the polygonal shape of the region inside the shear layer is more pronounced for $\beta < 0$, and less for $\beta > 0$. This

https://doi.org/10.1017/S0022112099004887 Published online by Cambridge University Press

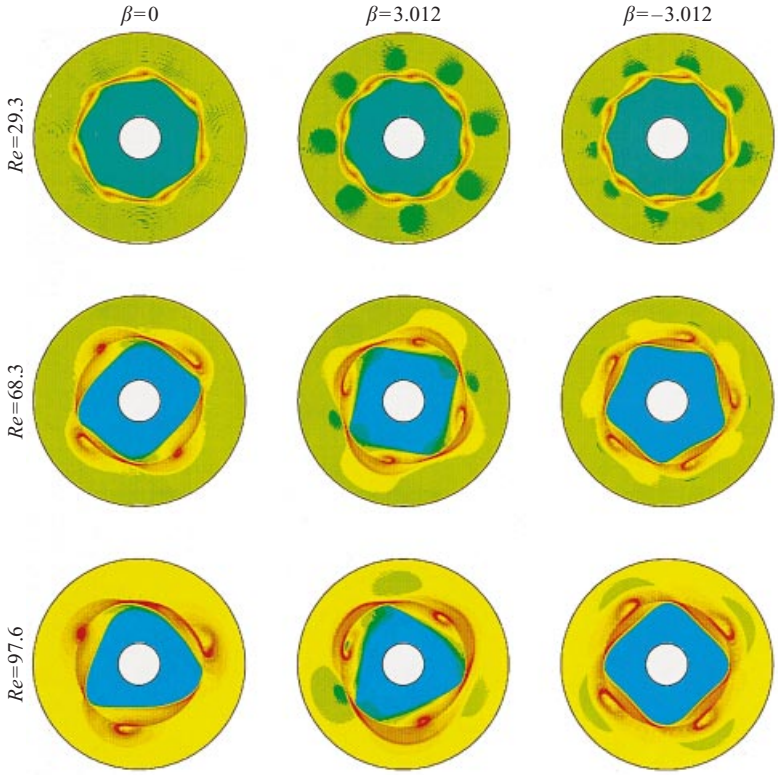


FIGURE 20. Vorticity distribution showing end states of nine numerical simulations. The rows correspond to different Re = 29.3, 68.3 and 97.6; the columns correspond to β = 0, 3.012 and −3.012 $\mathrm{CU}^{-1}\,\mathrm{s}^{-1}$.

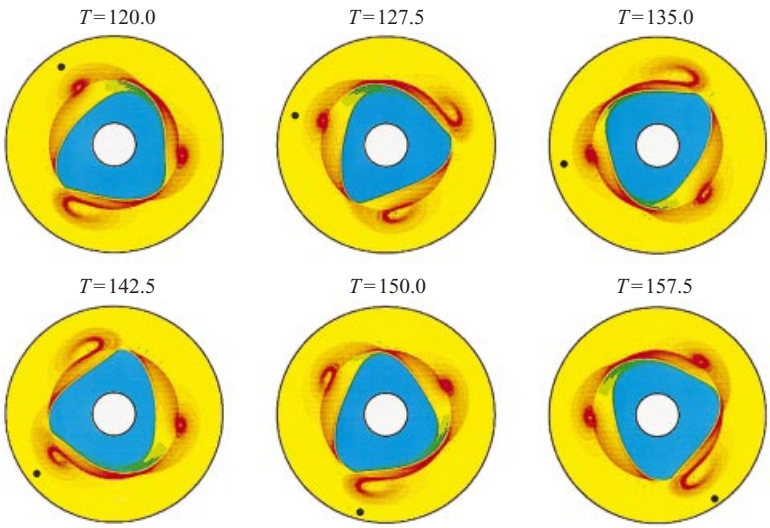


FIGURE 21. Evolution of the vorticity distribution of an unsteady mode 3. Parameters: $Re = 97.6$, $\beta = 0$.

https://doi.org/10.1017/S0022112099004887 Published online by Cambridge University Press

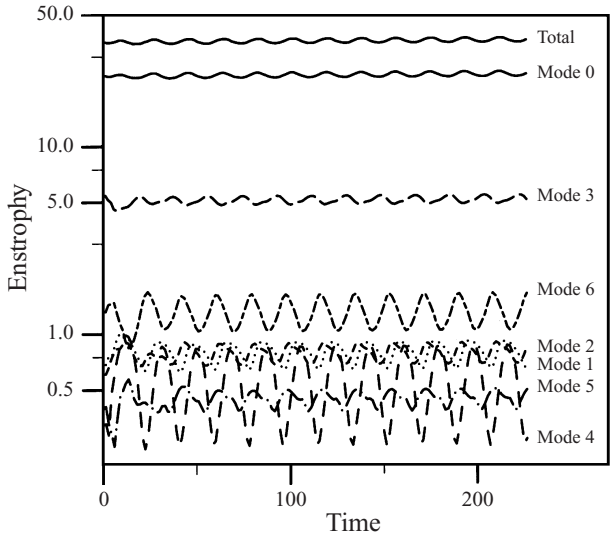


FIGURE 22. Enstrophy spectrum for the simulation of figure 21.

difference is explained by the conservation of potential vorticity $\omega - \beta r$, resulting in an increase in vorticity if a fluid element moves outward (toward a vertex of the polygon) if $\beta > 0$, and a similar decrease if $\beta < 0$. Similarly, the undulating motion of a fluid parcel induces a vorticity pattern outside the vortex chain. For $\beta > 0$ one observes an excess positive vorticity at the azimuthal location of the vortices, whereas for $\beta < 0$ positive vorticity appears between the vortices. The vorticity modulation induced by the β-effect may partially explain the stability properties of the vortex chain. For $\beta < 0$, the slightly concave shape of the inner region tends to separate the vortices, and thus leads to a greater stability, and therefore also to a higher mode number. Oppositely, the more circular inner region for $\beta > 0$ may enhance interaction between the vortices, and contribute to the more unstable nature of the vortex chain in that case.

Another observation in figure 20 (also made in the experiments) is that for high Reynolds number the vortices are unequal in size and shape. Generally, for five or more vortices present at the shear we obtain what can be called 'pure' modes, like that of figure 16. In contrast, figure 20 ($Re = 68.3$, $\beta = 0$) shows a state with four vortices that is not pure, since two of the vortices are perturbed. The enstrophy spectrum shows that a mode-2 component is also excited. Another complication can be seen in figure 20 ($Re = 97.6$, $\beta = 0$). In that case, the final configuration is no longer steady, but shows an oscillatory motion in which the three vortices vary in size and shape. This is seen in more detail in figure 21, which shows the evolution of the vorticity distribution during one period (note that there is a slight rotation of the whole system in the anticlockwise direction). The vortices appear to be affected by a perturbation propagating in the anticlockwise direction around the shear layer. This is clarified further by figure 22, which shows the enstrophy spectrum of the fully developed mode-3 flow. All the modes appear to be oscillating with the same frequency, mode 3 and 6 having the largest amplitude, followed by perturbations consisting of mode 2 and mode 1.

https://doi.org/10.1017/S0022112099004887 Published online by Cambridge University Press

7. Conclusions

First, our measurements confirm earlier observations about the shear layer on an f-plane. The stability of the shear layer is determined by the Reynolds number based on the thickness of the Stewartson $E^{1/4}$-layer. At low values of the Reynolds number, the shear layer is circular and stable, and corresponds to the case analysed by Stewartson. Above a critical Reynolds number, the shear layer becomes unstable, and is transformed into a number of discrete vortices. The number of vortices decreases with increasing Reynolds number, in agreement with the scaling argument proposed by Manin (1990). If the supercriticality is not too large, the vortex pattern is symmetric and steady. If the Reynolds number is high, the flow may become asymmetric or oscillatory.

Irrespective of the slope of the bottom the vortices appear to be aligned with the rotation axis, in agreement with the Taylor–Proudman theorem, but contrary to the rather common misconception that vortices should be perpendicular to the local normal as a consequence of the shallow-water approximation.

A β-effect appears to be stabilizing if the inner rotation is in the eastward direction, and leads to an unsteady vortex chain in the opposite case. A possible factor determining the difference between these situations is the shape of the region encircled by the vortices. Coupling to Rossby waves might provide another mechanism, but on closer inspection this seems to be unlikely; the measured velocity of the vortices always exceeds the maximum phase velocity of Rossby waves; moreover, the numerical simulations show no evidence of propagating waves.

The continuous adding of fluid in the centre and withdrawing it at the periphery leads to an azimuthal flow with a $1/r$-profile. If the shear of this profile is adverse to the direction of the inner rotation, the flow is considerably stabilized. In that case the amount of vorticity in the shear layer is unaffected, but the stretching effect of the differential rotation is counteracted by the shear of the pumping. Oppositely, if the azimuthal flow has the same sense as the inner rotation, the vortices become elongated, and fewer in number.

This work is supported by the Danish Natural Research Council (SNF) grant nr. 9600852 and by INTAS-RFBR 95-0988. The authors would like to thank R. de Nijs for his contribution in the initial phase of the investigations, and the referees for their useful comments.

REFERENCES

Beckers, M. & Heijst, G. J. F. van 1998 The observation of a triangular vortex in a rotating fluid. *Fluid Dyn. Res.* **22**, 265–279.

Bergeron, K., Coutsias, E. A., Lynov, J. P. & Nielsen, A. H. 1996 Self-organization in circular shear layers. *Physica Scripta* **T67**, 33–37.

Chomaz, J. M., Rabaud, M., Basdevant, C. & Couder, Y. 1988 Experimental and numerical investigation of a forced circular shear layer. *J. Fluid Mech.* **187**, 115–140.

Churilov, S. M. & Shukhman, I. G. 1992 Weakly nonlinear theory of the alternation of modes in a circular shear flow. *J. Fluid Mech.* **243**, 155–169.

Coutsias, E. A., Bergeron, K., Lynov, J. P. & Nielsen, A. H. 1994 Self organization in 2D circular shear layers. *AIAA Paper* 94-2407.

Coutsias, E. A. & Lynov, J. P. 1991 Fundamental interactions of vortical structures with boundary layers in two-dimensional flows. *Physica* D **51**, 482–497.

Dolzhanskiĭ, F. V., Krymov, V. A. & Manin, D. Yu. 1990 Stability and vortex structures of quasi-two-dimensional shear flows. *Sov. Phys. Usp.* **33** (7), 495–520.

Greenspan, H. P. 1968 *The Theory of Rotating Fluids*. Cambridge University Press.

https://doi.org/10.1017/S0022112099004887 Published online by Cambridge University Press

Heijst, G. J. F. van 1994 Topography effects on vortices in a rotating fluid. *Meccanica* **29**, 431–451.

Hide, R. & Titman, C. W. 1967 Detached shear layers in a rotating fluid. *J. Fluid Mech.* **29**, 39–60.

Hopfinger, E. J. & Heijst, G. J. F. van 1993 Vortices in rotating fluids. *Ann. Rev. Fluid Mech.* **25**, 241–259.

Kloosterziel, R. C. & Heijst, G. J. F. van 1991 An experimental study of unstable barotropic vortices in a rotating fluid. *J. Fluid Mech.* **223**, 1–24.

Leblanc, S. & Cambon, C. 1997 On the three-dimensional instabilities of plane flows subjected to Coriolis force. *Phys. Fluids* **9**, 1307–1316.

Manin, D. Yu. 1989 Stability of two-dimensional shear flows in the presence of the beta effect and external friction. *Izv. Akad. Nauk. SSSR, Atmos. Ocean. Phys.* **25** (8), 593–598.

Manin, D. 1990 Characteristic size of vortices in developed quasi-two-dimensional flows. *Izv. Akad. Nauk. SSSR, Atmos. Ocean. Phys.* **26** (6), 426–429.

McIntyre, M. E. 1989 On the antarctic ozone hole. *J. Atmos. Terr. Phys.* **51**, 29–43.

Nezlin, M. V. & Snezhkin, E. N. 1993 *Rossby Vortices, Spiral Structures, Solitons.* Springer.

Nielsen, A. H. 1993 Electrostatic turbulence in strongly magnetized plasmas. PhD thesis, Risø National Laboratory, R-659.

Niino, H. & Misawa, N. 1984 An experimental and theoretical study of barotropic instability. *J. Atmos. Sci.* **41**, 1992–2011.

Pedlosky, J. 1987 *Geophysical Fluid Dynamics.* Springer.

Rabaud, M. & Couder, Y. 1983 A shear-flow instability in a circular geometry. *J. Fluid Mech.* **136**, 291–319.

Stewartson, K. 1957 On almost rigid rotations. *J. Fluid Mech.* **3**, 17–26.

Trieling, R. R., Linssen A. H. & Heijst, G. J. F. van 1998 Monopolar vortices in an irrotational annular shear flow. *J. Fluid Mech.* **360**, 273–294.

Waugh, D. W., Plumb, R. A., Atkinson, R. J., Schoeberl, M. R., Lait, L. R., Newman, P. A., Loewenstein, M., Toohey, D. W., Avallone, L. M., Webster, C. R. & May, R. D. 1994 Transport out of the lower stratospheric Arctic vortex by Rossby wave breaking. *J. Geophys. Res.* **99** D, 1071–1088.

https://doi.org/10.1017/S0022112099004887 Published online by Cambridge University Press